CXRS measurements of energetic helium ions in ASDEX Upgrade plasmas heated with a three-ion ICRF scenario

A. Kappatou[1], M. Weiland[1], R. Bilato[1], Ye. O. Kazakov[2], R. Dux[1], V. Bobkov[1], T. Pütterich[1], R.M. McDermott[1], the EUROfusion MST1 team[*] and the ASDEX Upgrade team[+]

[1]Max-Planck-Institut für Plasmaphysik, Garching, Germany
[2] Laboratory for Plasma Physics, LPP-ERM/KMS, Brussels, Belgium
[*] See author list of "B. Labit et al 2019 Nucl. Fusion **59** 086020"
[+] See author list of "H. Meyer et al 2019 Nucl. Fusion **59** 112014"

E-mail: athina.kappatou@ipp.mpg.de

Abstract. Fast ion physics is an active field of research in the fusion community, but most studies focus on deuterium fast ions. The generation and investigation of energetic helium in present devices, however, provide significantly more insight on how the fast alpha particles produced from fusion reactions, will behave in future reactor plasmas. Fast helium ion populations can be measured with charge exchange recombination spectroscopy in the wings of the helium spectral line (He II n=4-3, 468.6 nm) providing information on their distribution function. Charge exchange recombination spectroscopy measurements of energetic ^{3}He ions, a first for ASDEX Upgrade, are presented. The ^{3}He ions are accelerated to high energies by a three-ion ICRF heating scenario in a mixed hydrogen-deuterium plasma. The spectral signature of the energetic helium ions in the charge exchange spectra is presented and compared with the theoretical predictions obtained with the TORIC-SSFPQL code. The magnitude of the predicted charge exchange spectral radiance, obtained via forward-modelling of the spectrum utilising TORIC-SSFPQL distribution functions, and the expected energies of the ions agree well with the measurement, confirming that the spectral feature is due to ICRF-accelerated ^{3}He ions. Comparisons between the experimental measurement and the modelling reveal discrepancies that illuminate details of the velocity distribution function of these ions.

Manuscript
28 October 2020

1. Introduction

Understanding the helium confinement and transport in a fusion plasma is critically connected to the performance and exploitation of current and future fusion devices. Poor confinement of alpha particles undermines the self-heating of the bulk plasma, while potentially causing damage to the plasma-facing components. At the same time, accumulation of thermalised fusion alpha particles reduces the fusion performance by diluting the fusion fuel. In this respect, diagnostic measurements of confined helium ions, both energetic and thermal, which provide information on their spatial and velocity distribution are highly desired. Diagnostic measurements of thermal helium have been available in many tokamaks and stellarators by means of charge exchange recombination spectroscopy. These are made by introducing helium, usually by gas puffing, helium neutral beams or helium glow discharges or wall coating processes such as boronisation. Fast ion physics is an active field of research in the fusion community, but most studies focus on deuterium fast ions. The generation and investigation of energetic helium ions in present devices, however, can provide insight on how fusion-generated, fast alpha particles will behave in future reactor plasmas.

Aside from investigating fusion-born α-particles (during D-T experiments in TFTR [1]), a fast helium population can be generated either by helium neutral beam injection (NBI) (JET [2]) or by using ion cyclotron resonance frequency (ICRF) heating to accelerate either ^{4}He-beam ions (JET [3]) or ^{3}He ions (TFTR [4]). A key element in such studies is the measurement of the fast helium populations with charge exchange recombination spectroscopy (CXRS), as presented in [1, 2, 4]. In this work, CXRS measurements of energetic helium ions, a new measurement for ASDEX Upgrade (AUG), are presented. The ^{3}He ions are accelerated to energies on the order of 1 MeV by a novel three-ion ICRF scenario [5] in a mixed H-D plasma. The spectral signature of these energetic helium ions in the CX spectra is described in Sec. 2. For the interpretation, the spectral radiance is modelled using distribution functions from the TORIC-SSFPQL code [6] and compared to the measurements in Sec. 3, providing a cross-validation between the diagnostic measurements and the ICRF modelling.

2. Spectral signature of energetic helium in AUG plasmas heated with the three-ion ICRF scenario

2.1. Charge exchange spectroscopy for measurements of thermal and energetic helium

CXRS is a routinely used plasma diagnostic that provides the impurity ion temperature, rotation and density, from the Doppler broadening, the Doppler shift and the intensity of the measured CX emission line, respectively. The most commonly used spectral line for helium measurements is at 468.571 nm, corresponding to the n=4-3 transition. The interpretation of the helium CX spectra is not straightforward. Assuming only thermal helium present in the plasma, the helium emission line is comprised of: a) the active charge exchange emission due to charge exchange reactions of fully-stripped He with beam neutrals, b) the passive emission, driven mainly by electron impact excitation of He^+ and by charge exchange of He^{2+} with thermal neutrals at the plasma edge, and c)

the "plume" emission [7], an additional emission due to electron collisional excitation of the He^+ ions produced by charge exchange reactions along the neutral beam. The active emission line has a Gaussian shape for thermal populations. The passive and "plume" emission lines, on the other hand, do not. The passive emission is optimally subtracted with beam modulation, while the "plume" emission needs to be modelled [8].

An energetic helium population with energies higher than the thermal population contributes an additional emission to the spectra, in the wings of the helium spectral line, at higher and/or lower wavelengths. The difficulty in measuring the spectral signature of energetic helium lies in the fact that the intensity of this emission is in most cases too low. The intensity of the signal depends on the amount of energetic ions in the plasma, their relative velocity with respect to the neutral beam used for the CXRS measurements, and the details of their distribution function. The detection limit is met when the energetic helium CX signal is equal to or lower than the Bremsstrahlung level (for a discussion of the signal-to-noise ratio for CXRS measurements see [2]). A "plume" emission due to the energetic helium population is negligible, as these He^+ ions are produced by charge exchange reactions and are born with high velocities such that they travel far along the field lines before they can be excited by electron impact [8, 9].

CXRS is one of the few diagnostics that can measure confined energetic α-particles (others being $\gamma-$ray spectroscopy, neutral particle analysers, collective Thomson scattering). The availability of information on the fusion produced helium ions in devices with D-T operation is highly desired. This underlines the importance of exercising, but most importantly, understanding the CXRS measurements of high energy helium populations. Furthermore, the diagnosis of high energy helium ions accelerated by radio-frequency waves in a variety of ICRF schemes is beneficial for the assessment of the efficiency of the heating scenario and the evaluation of the impact on the plasma performance.

2.2. Plasma scenario

An energetic helium signal was observed in the CX spectra in a variety of plasma pulses aimed at investigating the feasibility of a novel three-ion ICRF scenario at AUG [5, 10, 11]. The plasma discharge #34704 discussed herein was part of the first attempts to apply this novel heating scenario in mixed H-D plasmas ($n_H/n_e \sim 70-80\%$) on ASDEX Upgrade, using a small amount of ^{3}He ions as resonant ion species to absorb ICRF power. In this work, CXRS measurements of ^{3}He accelerated using this ICRF scenario are examined for the first time at AUG. References [10, 11] provide additional background on the success and application of such novel ICRF scenarios at ASDEX Upgrade.

An overview of the heating, fuelling, and plasma parameters of AUG plasma discharge #34704 ($B_t = -2.8$ T, $I_p = 0.8$ MA), used herein as an example, is given in Fig. 1. An important difficulty associated with the application of this heating scenario on AUG is controlling the desired ^{3}He concentrations ($c_{^3He}$) at low levels $\sim 0.5-2\%$, in the absence of a real-time control scheme. Core $c_{^3He}$ of 0.5-1% were achieved by short puffs (50 ms long, every 0.5 s, with a puffing rate of $2.3 \cdot 10^{20}$ e/s). Hydrogen neutral beams were used ($P_{NBI} \sim 8$ MW, 53 keV). The ICRF power was increased in steps 0, 0.9, 1.9 and

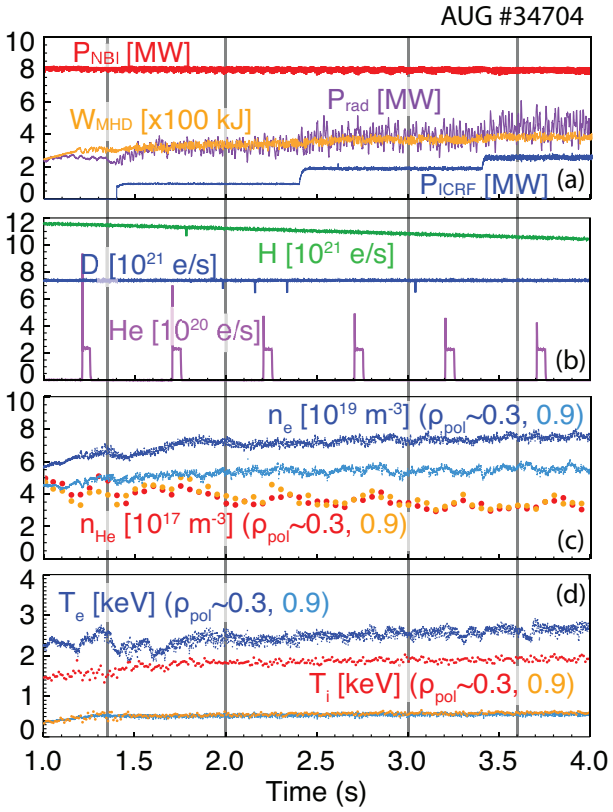

Figure 1: a) NBI, ICRF, stored energy and radiated power in the ASDEX Upgrade plasma discharge #34704 (0.8 MA/2.8 T, f=30 MHz ICRF, dipole phasing), b) D, H and ^{3}He electron puffing rates, c) electron and total helium (^{3}He and ^{4}He) densities, d) electron and ion temperatures at $\rho_{\rm pol} \sim 0.3$ and 0.9.

2.5 MW at a frequency of 30 MHz with dipole phasing. In this pulse, the fundamental ion-cyclotron resonance of ^{3}He was deliberately located at $\rho_{\rm pol} \sim 0.3$ on the high-field side, via the choice of the toroidal field, to reduce the fast ion energies and thus improve the confinement of the RF-heated ^{3}He ions. The option of high-field side off-axis ^{3}He heating with the three-ion heating scenario was suggested as a potential option for H-mode studies in ITER [12].

Examples of the measured helium charge exchange spectra in #34704 are shown in Fig. 2 in linear (a) and logarithmic (b) scale for one diagnostic line-of-sight (LOS) corresponding to $\rho_{\rm pol} \sim 0.3$. The time points correspond to the different levels of $P_{\rm ICRF}$ and are indicated by vertical lines in Fig. 1. The lines-of-sight used are toroidally oriented (more details on the observation geometry will be discussed in Sec. 2.4). The passive, "plume," and thermal active emissions are around the nominal He II wavelength (468.571 nm). The emission corresponding to the energetic ^{3}He population can be seen at wavelengths > 470 nm and < 468 nm. ^{3}He and ^{4}He cannot be distinguished in the CXRS measurements. Since the ICRF scenario applied here, however, accelerates efficiently mainly the ^{3}He ions, any signal corresponding to non-thermal He populations can be attributed to ^{3}He ions. Without ICRF, no energetic population is observed (red

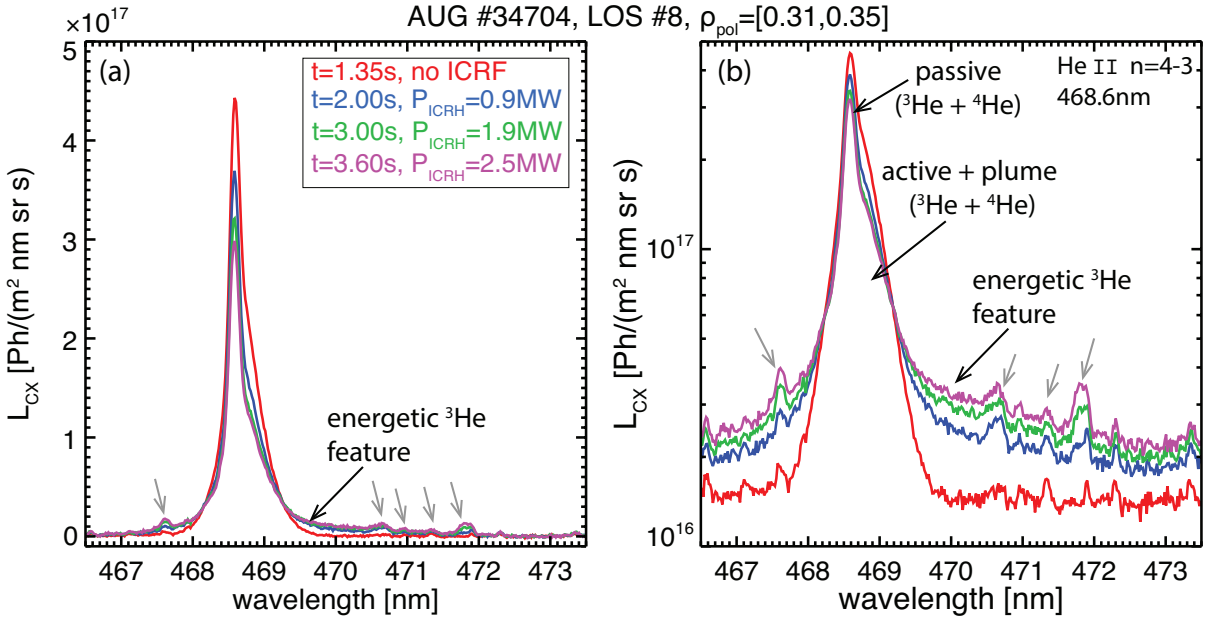

Figure 2: Measured CX spectra shown in (a) linear and (b) logarithmic scale for one line-of-sight at the different times and P_{ICRF} levels during #34704 indicated in Fig. 1. The grey arrows indicate the unidentified emission lines that overlap with and disturb the measurement of the energetic helium.

spectrum). With increasing P_{ICRF}, the intensity of the energetic helium emission increases (blue, green, and purple spectra).

Several smaller emission lines, most probably associated with tungsten, disturb the spectra (shown with grey arrows in the figure). The tungsten concentration in this pulse is in the range $c_W = 0.6\text{-}1.2 \cdot 10^{-4}$, and increases as the ICRF power is increased. While beam modulation can be used to minimise the impact of such disturbing emission lines, this was not available in this pulse. Due to these complications, and most importantly, because the exact shape of the energetic helium spectral feature is unknown, a complete fit of the spectra to separate the different helium spectral contributions cannot be performed with accuracy. Before continuing on to the analysis of the energetic helium spectral signature, a more careful look at the spectra is required.

2.3. Detailed analysis of the helium charge exchange spectra

The plasma discharge #34704 is optimal to illustrate the features of the energetic ^{3}He spectral signature, mainly due to the scan in P_{ICRF}. However, the spectra measured for this pulse are polluted by many smaller emission lines. To allow for an accurate and fair comparison against modelled data (see next section), a very careful treatment of the spectra is necessary. This involves the removal of the emission lines that disturb the measurement of interest, as well as an accurate identification of the Bremsstrahlung level in the spectra.

The wavelengths of the majority of these disturbing emission lines cannot be easily identified so that they can be fitted with a combination of Gaussian line shapes in the spectra. Furthermore, their intensities and exact wavelength positions are observed to

change in time and from the core to the edge of the plasma. The hypothesis is that these emission lines correspond to different charge states of tungsten, the level of which increased as the ICRF power was increased in steps. These emission lines are not observed in the helium charge exchange spectra when the W concentration is sufficiently low. Other elements cannot be excluded either to be responsible for these emission lines. In this work, emphasis was placed on identifying the wavelength ranges in which they appear and removing them from the spectra, so that they do not influence the analysis, rather than on the detailed identification of the element and charge state from which they arise.

The disturbing lines with the strongest intensities are identified by determining the wavelength ranges in which the smoothed, normalised, second-derivative of the spectral radiance becomes strongly negative, as illustrated in Fig. 3. The variation of the normalised first derivative of the spectral radiance around these points allows for the identification of the wavelength in which the emission line is present. While this procedure is sufficient to remove the strongest of these lines, a number of smaller emission lines might still be present. By examining the spectra from multiple locations in the plasma at multiple time points, the wavelength range $\lambda = 472.5 - 472.9$ nm, on the right hand side of the energetic ^{3}He feature, was identified to be free of disturbing emission lines. This wavelength region is indicated by the green box in Fig. 3. At this wavelength range the energetic ^{3}He signal is expected to be very low. The corresponding background level defined as the average of the spectral radiance in this wavelength range is shown with a green horizontal line.

However, an overview of the complete measured spectrum reveals that the minimum of the spectral radiance is lower than this value. In the example shown, this minimum is observed at $\lambda \sim 462.4$ nm (identified with an orange box in the figure). This level is lower than the one calculated from $\lambda = 472.5 - 472.9$ nm by 14% (note the logarithmic scale of the y-axis). The real Bremsstrahlung level is at least as low as this minimum spectral radiance. Yet, the presence of many, less intense emission lines across almost the complete measured wavelength range is better captured by the level defined by the measured radiance at $\lambda = 472.5 - 472.9$ nm.

In Fig. 4, the background levels obtained with the two methods are compared for four different time points in the pulse, corresponding to different ICRF power levels, and for a subset of the lines-of-sight. The background spectral radiance is measured integrated along the path of each line-of-sight, but they are plotted against the ρ_{pol} corresponding to the measurement location of each line-of-sight (crossing point with the neutral beam path), for easier inspection. It is observed that the two methods are different by maximum $\sim 15\%$ up to $\rho_{\mathrm{pol}} \sim 0.8$ and have the same trend across the plasma radius. The expected Bremsstrahlung for all lines-of-sight is calculated utilising an independent measurement of Z_{eff} (as well as n_e and T_e profiles). A Z_{eff} value, constant across the plasma radius, is obtained by means of Integrated Data Analysis in the framework of Bayesian probability theory [13], based on the Bremsstrahlung measurements of another CXRS system which was measuring at the boron wavelength (around 494.5nm). The Z_{eff} uncertainty is not small and leads to a large uncertainty in the Bremsstrahlung emission (not shown). The predicted Bremsstrahlung emission, integrated along each line-of-sight,

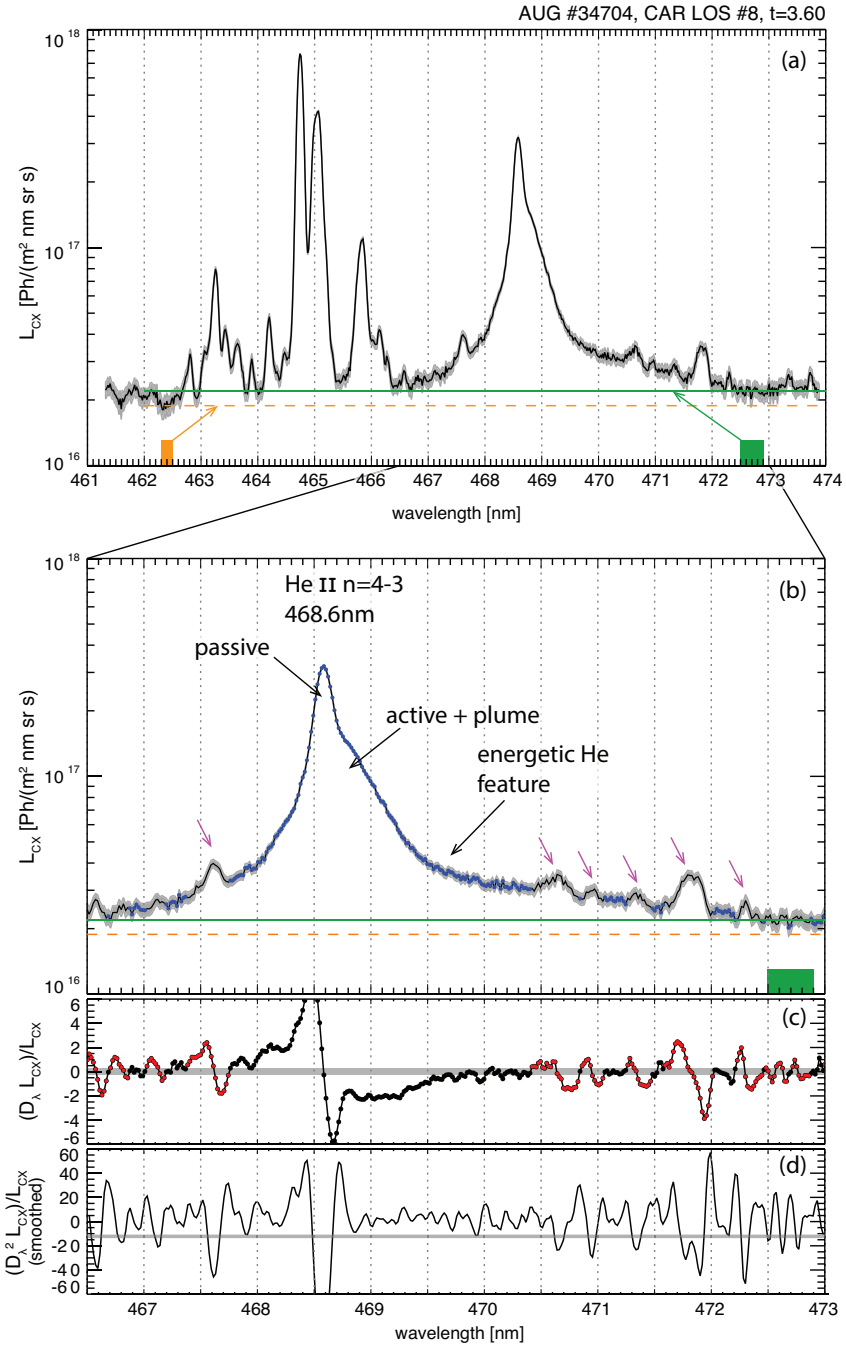

Figure 3: (a) Measured CX spectra for LOS #8 at 3.60 s in #34704. The background level defined as the average of the spectral radiance in $\lambda = 472.5 - 472.9$ nm (solid green line) and as the minimum of the spectral radiance (dashed orange line) are shown, b) the selected parts of the spectrum are identified with blue points. The disturbing emission lines, some of which are indicated with magenta arrows, are identified by investigating the normalised (c) first and (d) second derivatives of the measured spectral radiance.

provides an additional confirmation of the trend of the background levels defined with the two methods across the plasma radius.

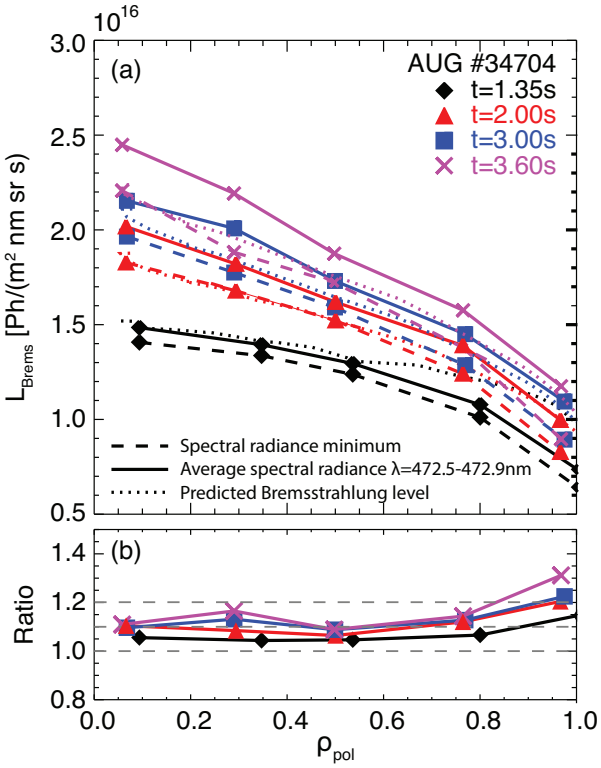

Figure 4: a) The background levels defined as the average of the spectral radiance in $\lambda = 472.5 - 472.9$ nm (——), as the minimum of the spectral radiance (- - - -) shown for 5 different lines-of-sight and at four time points in the pulse (varying P_{ICRF}) against the measurement location of each line-of-sight, together with the predicted Bremsstrahlung measured for all the lines-of-sight, based on an independent measurement of Z_{eff} (·····), b) the ratio of the two background levels.

The background level defined by the average over $\lambda = 472.5 - 472.9$ nm is chosen for the background subtraction. It allows for a better treatment of smaller emission lines which are potentially present below the whole spectrum (across the wavelength range), in particular below the energetic ^{3}He feature, as identified in the spectra measured at different time points and plasma locations. The presence of such emission lines can justify the small difference of up to 15% between the background level obtained with the two methods.

2.4. Measured charge exchange spectral radiance associated with energetic helium ions

The measured radial profiles of the energetic ^{3}He CX radiance are investigated to reveal the characteristics of the energetic ^{3}He population for the different ICRF power levels.

In Fig. 5(a), the CX spectral radiance is plotted as a function of the energy of the ions along the line-of-sight, defined from the velocity component projected on the line-of-sight in the direction of the field lines (ions moving away from the observer), for the different time points and P_{ICRF} levels indicated in Fig. 1. Wavelength ranges with $\lambda > 469.5$nm are

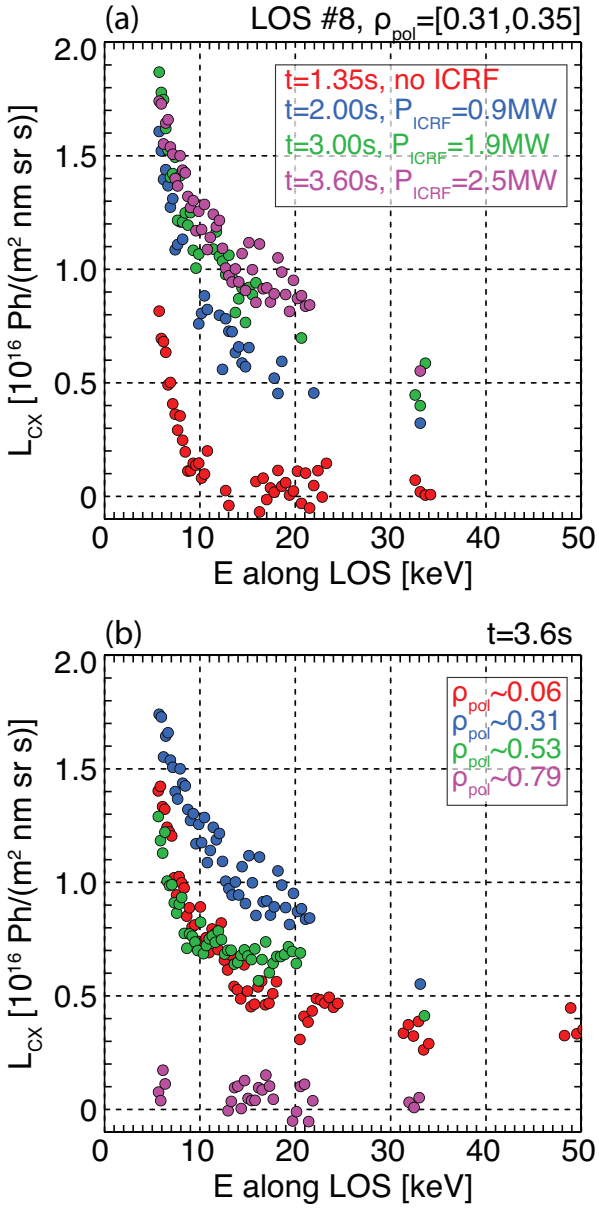

Figure 5: CX spectral radiance as a function of the ion energy projected onto the line-of-sight (LOS), a) at the time points shown in Fig. 2 at $\rho_{pol} \sim 0.3$ (the variation in ρ_{pol} arises from the equilibrium evolution in time) and b) across ρ_{pol} at $t = 3.6\ s$

used for the plots in Fig. 5. The disturbing emission lines are avoided as described in 2.3. The wavelength range $\lambda = 472.5 - 472.9$ nm is used for the background subtraction.

The uncertainty on the measured CX spectral radiance L_{CX} shown on the spectrum in Fig. 3 encompasses the photon noise as well as the read-out noise of the camera and is $< 10\%$. The intensity sensitivity of the CX system (spectrometer, fiber optics, and in-vessel components) is well characterised and its uncertainty is on the order of 10%. Therefore, an uncertainty of up to $\sim 0.15\%$ should be considered for the measurements shown in Fig. 5 (not shown). Deterioration of the in-vessel components due to material coating and radiation during an experimental campaign contributes further to

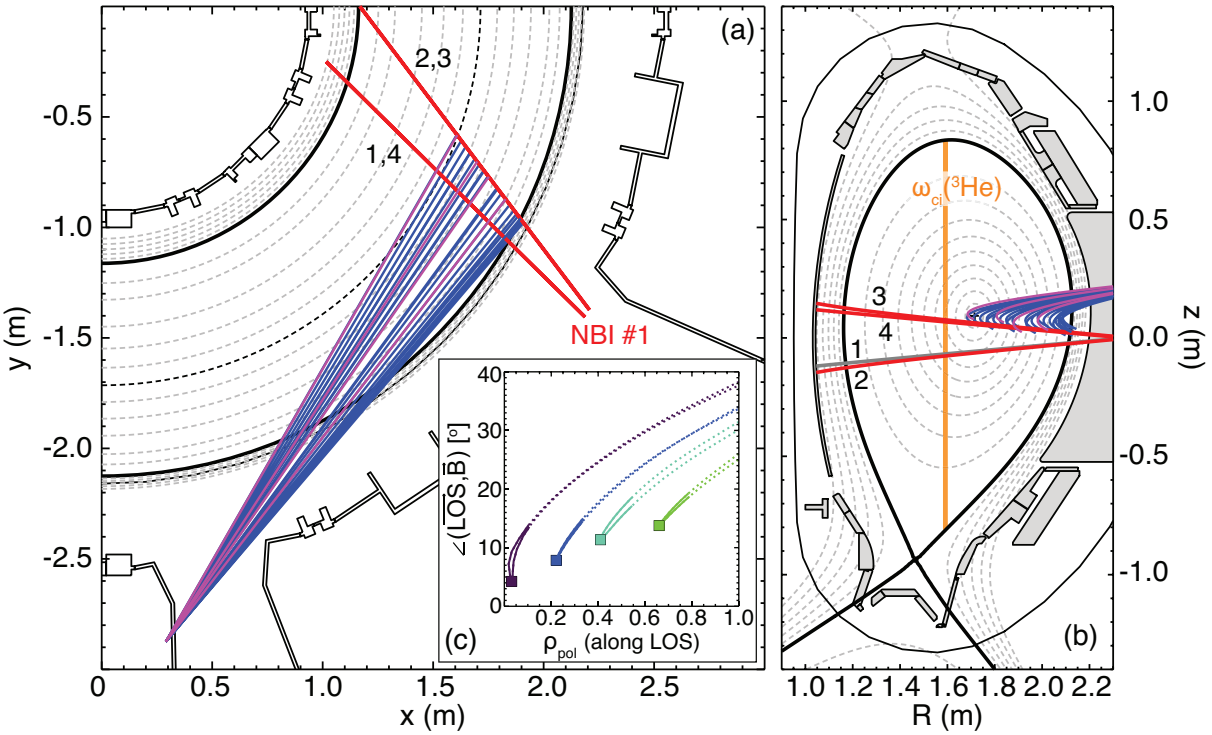

Figure 6: The lines-of-sight of the system measuring the helium CX spectra a) in a top-down view and b) in the poloidal cross-section of AUG. The lines-of-sight used herein are identified with magenta color. The neutral beam sources #2-#4 of NBI box 1 are on in this pulse (red). The equilibrium shown is from #34704 at 3.0 sec. The ^{3}He resonance is indicated. The angles between the selected line-of-sights with the magnetic field are shown in the inset (d) for the path along each line-of-sight, with the solid part of the lines indicating the part of the line-of-sight through the $1/e$-width of the neutral cloud.

the intensity calibration uncertainties. It should be noted, however, that these processes affect all lines-of-sight of the system in the same way. This has been verified via post-campaign calibrations over multiple campaigns.

The observation geometry is important in understanding the value of the energy (velocity) along the line-of-sight. The CXRS system has a toroidal view on the AUG NBI box I and is focused on source #3, but intersects all NBI box I sources (in this pulse, sources #2-#4 were on). The geometry of the CXRS lines-of-sight can be seen in Fig. 6. The lines-of-sight used in Fig. 5 are indicated with magenta color. The angles of the lines-of-sight to the magnetic field lines are shown in the inset for a subset of the lines-of-sight. The squares show the minimum angle of the lines of sight to the magnetic field lines which is $< 15°$, while the solid part of the lines indicates the part of the line-of-sight that crosses the $1/e$-width of the neutral cloud. As such the lines-of-sight sample predominantly the velocity of the ions parallel to the magnetic field, but see very little of the perpendicular velocity, which is expected to be increased the most for RF-accelerated ions.

The measured energetic signal corresponds to ions with energies larger than ~ 10 keV projected on the line-of-sight, i.e. $E_{LOS} > 10$ keV. The spectral radiance is correlated with the ICRF power level, while there is no energetic ^{3}He spectral signature when ICRF is not applied. The spectral radiance depends on the density of the energetic ^{3}He ions at that

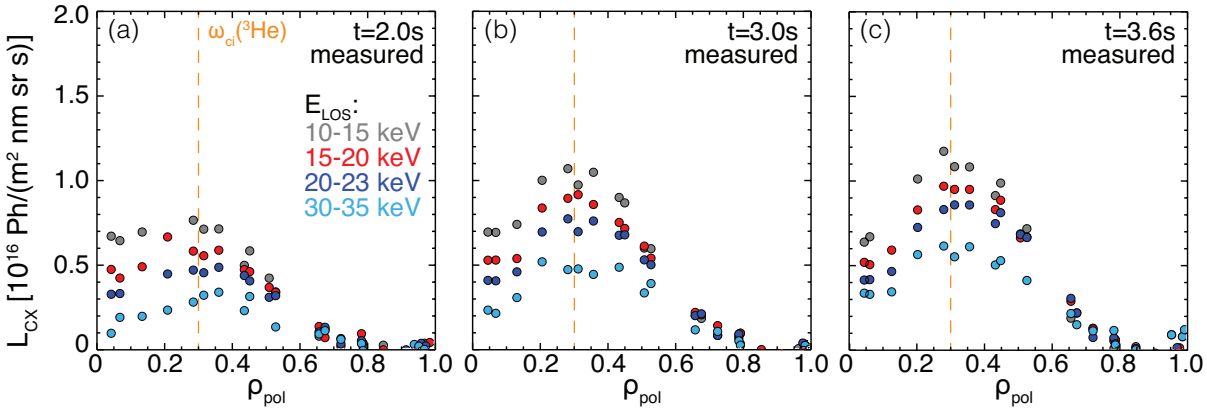

Figure 7: Radial profile of the CX spectral radiance integrated over various ranges of the ion energy projected onto the line-of-sight (E_{LOS}), for the three time points with increasing P_{ICRF}. The location of the ^{3}He RF resonance (on the high-field side) is indicated with the vertical dashed line.

location, but also on the background plasma parameters and the details of the velocity distribution of the ions.

In Fig. 5(b), the measured CX spectral radiance at t = 3.6 s is shown for different plasma locations (the corresponding lines-of-sight are identified in Fig. 6). The signal is higher at $\rho_{pol} \sim 0.3$ and lower towards the magnetic axis and the plasma mid-radius. At the outer part of the plasma, no CX signal corresponding to the energetic ^{3}He ions is observed. The population of the energetic ^{3}He ions is shown to be present inside the inner half of the plasma radius, with the majority of them at the resonance location of the ICRF waves. This is only the part of the population that can be observed by the CXRS measurements: more ^{3}He ions exist in the plasma, but have much higher energies (or high velocities in the perpendicular direction) that cannot be measured, as the CX emission rates reduce strongly at higher ion energies and the signal becomes too small with respect to the Bremsstrahlung background. The radial profile of the CX radiance integrated over different E_{LOS} ranges is shown in Fig. 7 for the three time points also shown in the previous figure. With increasing P_{ICRF}, more and more energetic helium ions are observed, in particular around the resonance location at $\rho_{pol} \sim 0.3$.

Obtaining the density of the energetic ^{3}He ions from these measurements is in principle possible, as is the evaluation of impurity densities from CXRS measurements. However, such a method cannot be directly applied as the population is not thermal and the velocity distribution non-Maxwellian. In the case of neutral beam fast ions, the Fast-Ion D_α (FIDA) spectra can be modelled once the solution for the velocity-space distribution of neutral beam fast ions is obtained [14, 15]. In the next section, an analogous approach is followed to forward model the CX spectra measured in the presence of ICRF accelerated ^{3}He ions.

3. Forward modelling of the charge exchange spectra using distribution functions obtained from TORIC-SSFPQL

3.1. Evaluation of the charge exchange spectral radiance

While obtaining the distribution function of the ^{3}He ions from the CXRS measurement is not straightforward, the expected spectral radiance L_λ can be evaluated as follows, if the velocity distribution function of the ^{3}He ions $f_{^3\mathrm{He}}(\upsilon, p)$ is available:

$$L_\lambda = \frac{1}{4\pi} \sum_{E=1}^{3,halo} \sum_{n=1}^{2} \int_{\upsilon=0}^{\upsilon_{max}} \int_{p=-1}^{1} \int_{\phi=0}^{2\pi} \upsilon^2 f_{^3\mathrm{He}}(\upsilon, p)\, \sigma_{\mathrm{CX}}(\upsilon_{col}^{E,n}) \upsilon_{col}^{E,n} \int_{LOS} n_b^{E,n}(l)\, \mathrm{d}l \times \delta\left[\lambda - \lambda_0 \left(1 + \frac{\upsilon}{c} \cos\theta\right)\right] \mathrm{d}\phi\, \mathrm{d}p\, \mathrm{d}\upsilon. \quad (1)$$

Here, λ corresponds to the wavelength and λ_0= 468.571 nm to the nominal wavelength of the He II emission line (n=4-3 transition). The integration is performed over the velocity υ and over the pitch angles $p = \cos(\upsilon_\parallel/\upsilon)$. The density of the beam neutrals $n_b^{E,n}$, where E corresponds to the three beam energy components and the beam halo and n to the main quantum number of the neutrals, is calculated with the collisional-radiative model used within the impurity density analysis code CHICA [16]. The fast ion velocity has a pitch angle p to the magnetic field line and an angle ϕ to the other perpendicular direction to the field line (gyro angle). θ is the angle between the line-of-sight and the ion velocity.

The distribution function at the effective measurement location of the line-of-sight is considered, and it is assumed that the distribution function, the local plasma parameters, and consequently the CX emission rates do not vary strongly along the path of the LOS through the neutral beam. Only $n_b^{E,n}$ is integrated along the CXRS line-of-sight with coordinate l. For the line-of-sight measuring at $\rho_{\mathrm{pol}} \sim 0.79$ in #34704 at 3.6 s, the following variations of the plasma parameters are observed along the line-of-sight: $^{\Delta T_i}/_{\mathrm{T_iLOS}} < 15\%$, $^{\Delta T_e}/_{\mathrm{T_eLOS}} < 16\%$, $^{\Delta n_e}/_{\mathrm{n_eLOS}} < 4\%$, $^{\Delta v_\phi}/_{\mathrm{v_\phi LOS}} < 13\%$, calculated on the $^1/_{\mathrm{e}}$-width of the neutral cloud. These variations are even smaller for lines-of-sight intersecting the neutral beams closer to the plasma core. Though not specifically addressed in the equation above, the spectral radiance is a sum of the contributions from the different neutral beam sources that are intersected by the lines-of-sight, and as such $n_b^{E,n}$ corresponds to the neutral densities of all neutral beams injected in the plasma.

The effective charge exchange emission cross-sections σ_{CX} depend on the collision velocity $\upsilon_{col}^{E,n}(\upsilon, p, \phi)$ between the ion (of velocity υ, pitch p and gyro angle ϕ) and the beam neutral (of energy E and main quantum number n). The dependence on p and ϕ are not important for the thermal halo neutrals. The effective emission cross-sections used, produced as described in [16], are plotted in Fig. 8. The full energy of the hydrogen neutral beam and the maximum collision energies per amu for the case that a 50 keV or a 250 keV ^{3}He ion is moving against the 53 keV beam neutrals are indicated. As the ions gyrate around the magnetic field lines, all collision energies from zero to this maximum are possible, depending on the gyro-angle. The $n = 1$ cross-sections are available for beam energies up to 300 keV (and up to 100 keV for $n = 2$), which is sufficient for the goal described herein. The effective cross-sections exist for the relevant electron densities

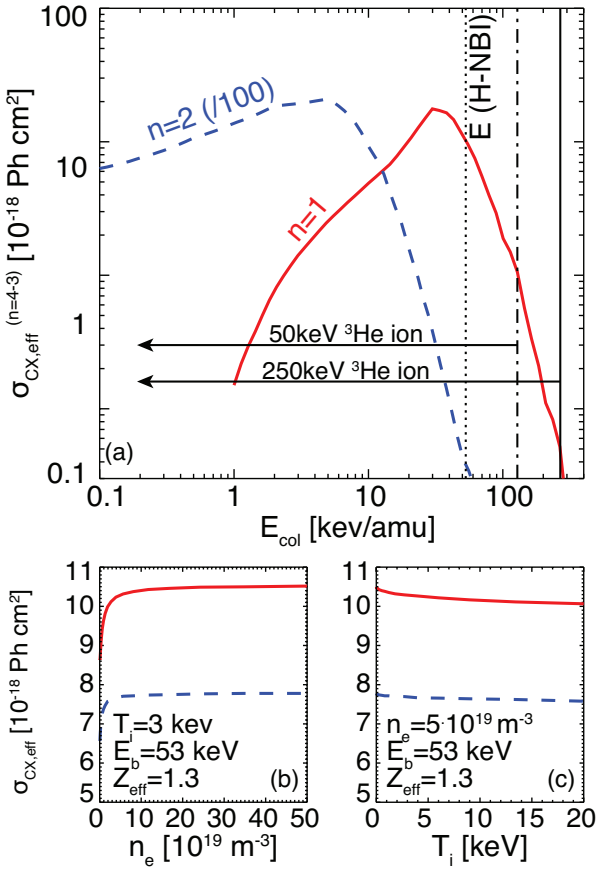

Figure 8: Effective charge exchange emission cross sections used, as a function of the a) neutral beam energy, indicating also the full energy of the hydrogen neutral beam (53 keV, ·····) as well as the maximum collision energies between a 50 keV (- · - · -) or a 250 keV ^{3}He ion (——) and the 53 keV hydrogen beam, b) electron density and c) ion temperature.

and effective charge values for an AUG plasma. The maximum ion temperature for which these atomic data are available is 20 keV, which is low in comparison to the energies of the RF-accelerated ^{3}He ions. The ion temperature is important for properly taking into account the l-mixing collisions with ions. Nevertheless, the variation of the effective cross-sections is only a few percent from 0.01 to 20 keV, therefore, the value for the maximum ion temperature available was used. The l-mixing collisions become less effective for ^{3}He ions of much higher energy. The photon emission cross-sections obtained using slow 1 keV ^{3}He and fast 500 keV ^{3}He ions for the calculation of the l-mixing collisions were compared and only very small differences were found.

To assess the pitch-velocity space to which the lines-of-sight are sensitive to, weight functions $W(\lambda, \upsilon, p)$ can be produced for each line-of-sight so that:

$$L_\lambda = \int_{\upsilon=0}^{\upsilon_{max}} \int_{p=-1}^{1} W(\lambda, \upsilon, p)\ \upsilon^2\ f_{^3\mathrm{He}}(\upsilon, p)\, \mathrm{d}p\, \mathrm{d}\upsilon, \tag{2}$$

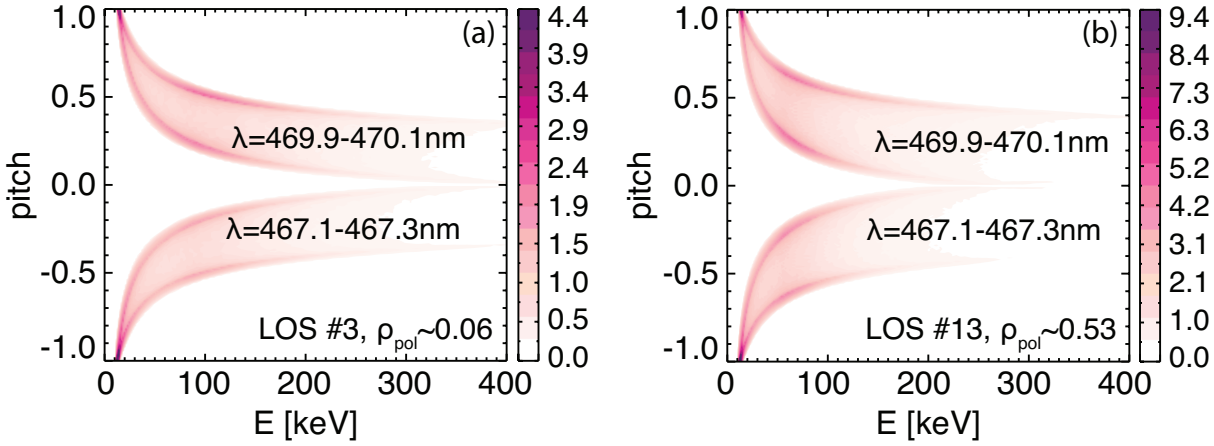

Figure 9: So-called weight functions illustrating the part of the velocity-pitch space that each line-of-sight samples, shown here for two example lines-of-sight in #34704 at t=3.6 s and for two wavelength ranges $\lambda_0 \pm 1.4$ nm, averaged over 0.2 nm. The maximum energy of 400 keV corresponds to a velocity of 5044 km/sec.

as is often done for FIDA measurements of fast deuterium ions. Weight functions of this type are presented and used, among others, in [14, 17]. From Eq. (1) the following expression is derived for the weight function:

$$W(\lambda, \upsilon, p) = \frac{1}{4\pi} \sum_{E=1}^{3,halo} \sum_{n=1}^{2} \int_{\phi=0}^{2\pi} \sigma_{\mathrm{CX}}(\upsilon_{col}^{E,n}) \upsilon_{col}^{E,n} \int_{LOS} n_b^{E,n}(l)\, \mathrm{d}l \times \delta\left[\lambda - \lambda_0 \left(1 + \frac{\upsilon}{c} \cos\theta\right)\right] \mathrm{d}\phi. \tag{3}$$

For the fast helium measurements presented herein, weight functions are calculated using the above equation for all gyro angles and are illustrated in Fig. 9 for two lines-of-sight. They enable an overview of the part of the phase-space that a line-of-sight samples. The weight functions are shown averaged for a specific wavelength range left or right of the nominal wavelength of the helium emission line corresponding to different Doppler-shifts. It should be underlined that this definition for the weight functions does not take into account the signal-to-noise ratio limits below which the measurement is not possible, or the fact that parts of the wavelength range might not be usable due to the presence of other emission lines.

3.2. Distribution functions of energetic ^3He ions from TORIC-SSPFQL

To model the spectral radiance of the CX spectra utilising Eq. (1), the TORIC-SSFPQL code is used to obtain the velocity distribution function of the ^{3}He ions accelerated by ICRF. TORIC is a full-wave code for simulating the propagation and absorption of electromagnetic waves in the ion cyclotron range of frequencies in axisymmetric plasmas [18]. The SSFPQL code is a quasilinear solver of the Fokker-Planck equation in the presence of ICRF and NBI sources [19]. TORIC-SSFPQL [6] couples the two solvers, allowing the numerical simulation of ICRF in the presence of NBI heating. The

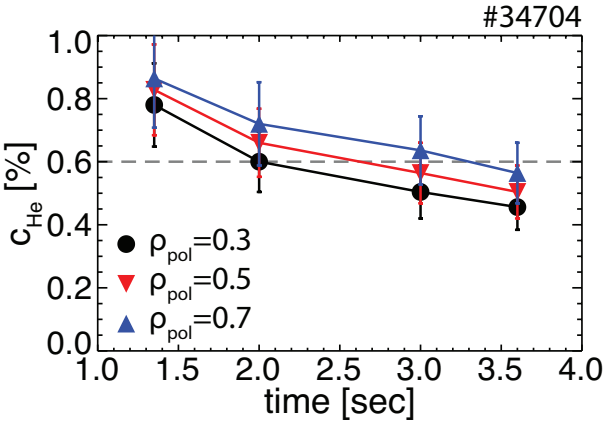

Figure 10: Total ^{3}He and ^{4}He concentration $c_{He} = (n_{^3He} + n_{^4He})/n_e$ derived ignoring the energetic tails in the spectrum, for three plasma locations during #34704.

simulations were performed taking into account the full toroidal mode spectrum of the ICRF antenna. No orbit losses and broadening or redistribution of the profiles were considered.

The details of the fast ^{3}He distribution function depend critically on the exact ^{3}He concentration, which is difficult to pinpoint in this situation. First, the appearance of disturbing emission lines makes the fitting of the charge exchange spectra more uncertain. Second, the ^{3}He concentration is obtained considering only the "thermal" part of the spectrum without the energetic tails, keeping the assumption of a thermal distribution function. Third, CXRS cannot distinguish between ^{3}He and ^{4}He. The helium concentration derived with these constraints is shown in Fig. 10 in time during #34704 and for three plasma locations (the error bars on the concentration involve only the error on the helium density and not the electron density). It varies slightly during the pulse and the helium density is found to be slightly less peaked than the electron density. The accuracy of the derivation is, however, too low to draw strong conclusions on the peaking of the helium density profile. The values correspond largely to the thermal ^{3}He and ^{4}He populations and ignore the helium ions accelerated to higher energies. The energetic population in the inner half of the plasma radius is not reflected in these values. The simulations were started assuming a ^{3}He concentration $c_{^3He} = n_{^3He}/n_e = 0.6\%$, which is approximately the value measured in the outer half of the plasma radius at 3.6 s. The complete ^{3}He density profile cannot be derived without knowing the amount of non-thermal ions and the amount of ^{4}He ions present in the plasma. Furthermore, it is not straightforward to model the helium spectra in their entirety, due to the number of different contributions and the additional emission lines. For these reasons, the assumed $c_{^3He} = 0.6\%$ is only an estimate provided for the simulations. The effect of the assumed $c_{^3He}$ will be discussed in Section 3.3. The assumed total ^{3}He density and the measured total He density, capturing only the thermal ions, can be seen in Fig. 11(c) for one time point. The error band on the measured helium density reflects the error on the helium density itself and the error of the spline fit to the measurement points.

TORIC-SSFPQL treats with a degree of approximation the banana orbits of the particles, comprised of their oscillation on a magnetic surface between the tips of the banana orbits, and the radial drifts responsible for the finite width of the banana orbits. SSFPQL solves the Fokker-Planck equation in the zero-orbit-width approximation, in other words the ions move only on a flux surface and the radial drifts are ignored. The distribution function is solved at one poloidal point (typically the LFS). The pitch-dependence of the RF-diffusion operator is modified in such a way as to mimic the orbital movement, assuming magnetic moment conservation.

The parallel and perpendicular temperature of the TORIC-SSFPQL distribution function for #34704 at t=3.6 s, $T_{\parallel}$ and $T_{\perp}$, respectively, can be seen in Fig. 11, in comparison to the background plasma ion temperature T_i. In the top plot, the TORIC-SSFPQL simulations were performed assuming a zero-width banana orbits (ZOW) of the energetic ^{3}He ions. The CXRS lines-of-sight are toroidal with angles $< 20°$ to the magnetic field and sample predominantly $T_{\parallel}$ which reaches up to 15 keV and to a lower degree the $T_{\perp}$, which reaches up to ~ 0.5 MeV. The $T_{\parallel}$ and $T_{\perp}$ values sampled by the lines-of-sight used in Fig. 5(b) are indicated by full and open circles, respectively.

With the zero-orbit-width assumption, an energetic signal is expected only in the region $0.15 < \rho_{\rm pol} < 0.55$. However, the CX measurements indicate energetic ^{3}He also close to the plasma axis, as seen in Fig. 5(b). Since the ICRF resonance, in this case, is at $\rho_{\rm pol} = 0.3$ on the high field side ($B_t = -2.8$ T), many trapped energetic particles resonating with the ICRF waves might have orbits with banana widths large enough to explore also the region close to the magnetic axis. For this reason, TORIC-SSFPQL simulations in which orbit effects are included were also performed. This is done by averaging the RF absorbed power deposition profile over the finite-width-orbits (FOW), by considering a set of representative orbits. The $T_{\parallel}$ and $T_{\perp}$ are shown in Fig. 11(b). It now becomes obvious that energetic ^{3}He should be measured at all radii inside $\rho_{\rm pol} < 0.7$, as seen in the CX measurements. The corresponding energetic ^{3}He density, defined as that of ions with energies exceeding 10 keV is shown in Fig. 11(c) for both assumptions, compared to the total helium density assumed as input to the modelling. In this case, almost all ^{3}He ions in the plasma region $0.2 < \rho_{\rm pol} < 0.5$ are accelerated to energies beyond 10 keV according to the modelling. This offers an explanation for the fact that the thermal helium density profile is less peaked than the electron density in the plasma core, as the higher energy helium ions are not considered in the derivation of $n_{\rm He,thermal}$ (total ^{3}He and ^{4}He), however, radial transport effects cannot be excluded.

The distribution function at 3.6 s ($P_{\rm ICRF} = 2.5$ MW), obtained with TORIC-SSFPQL with finite-orbit-width effects is shown in Fig. 12(a) for $\rho_{\rm pol} = 0.3$. The characteristic 'rabbit-ear' shape can be distinguished. The same distribution function is shown for two different pitch angles in plots (b) and (c), namely for zero pitch angle, corresponding to the ion velocities perpendicular to $\overrightarrow{B}$ (solid lines) and for p=0.985 (dashed lines) which corresponds to approximately 10° between the ion velocities and $\overrightarrow{B}$, similar to the angle with the lines-of-sight. In Fig. 12(b) the distribution function at 3.6 s can be seen for different $\rho_{\rm pol}$ locations in the plasma. For comparison, the corresponding Maxwellian distributions are also shown. In Fig. 12(c), the same is shown for one plasma location in time, which illustrates the evolution of the high-energy tail with increasing $P_{\rm ICRF}$. Note

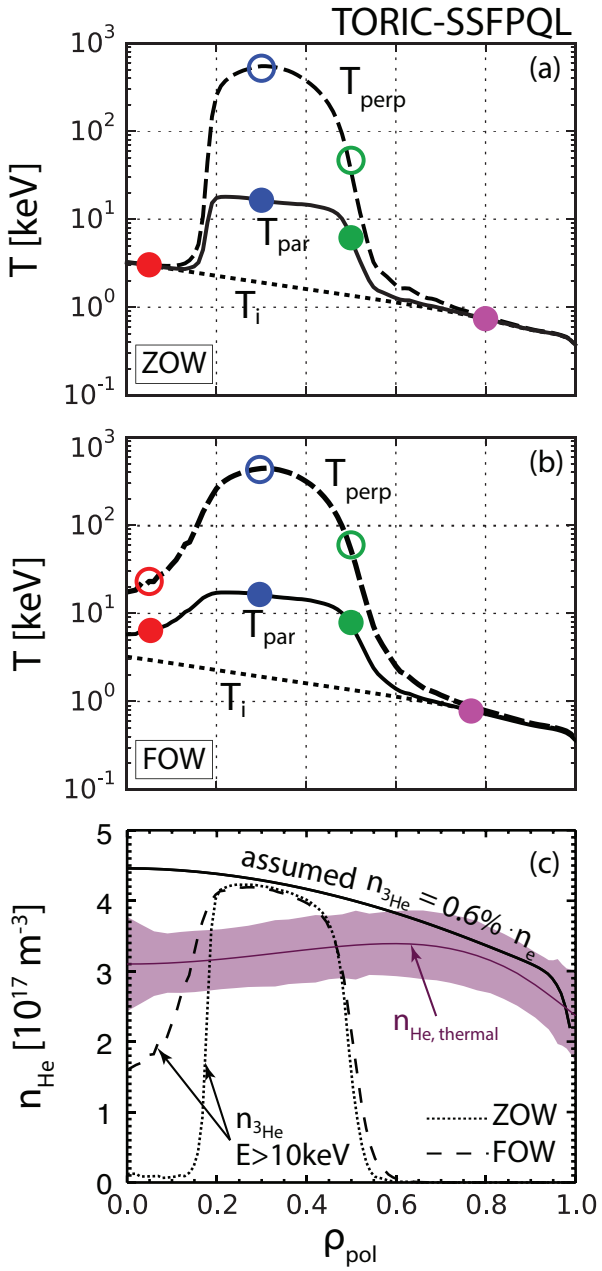

Figure 11: Parallel and perpendicular temperature of the ^{3}He distribution function obtained with TORIC-SSFPQL for #34704 at t=3.6 s, (a) with an assumption for a zero orbit width for the banana orbits of the energetic ^{3}He ions (ZOW) and (b) with an estimate for finite orbit width effects (FOW). The $T_{\parallel}$ and $T_{\perp}$ values sampled by the lines-of-sight used in Fig. 5(b) are indicated by full and open circles, respectively. The energetic ^{3}He densities with $E > 10$ keV are shown in (c) for both assumptions, together with the measured (thermal only) helium densities (^{3}He and ^{4}He).

that here, the thermal velocity, indicated with a vertical grey line, varies only marginally for the different time points.

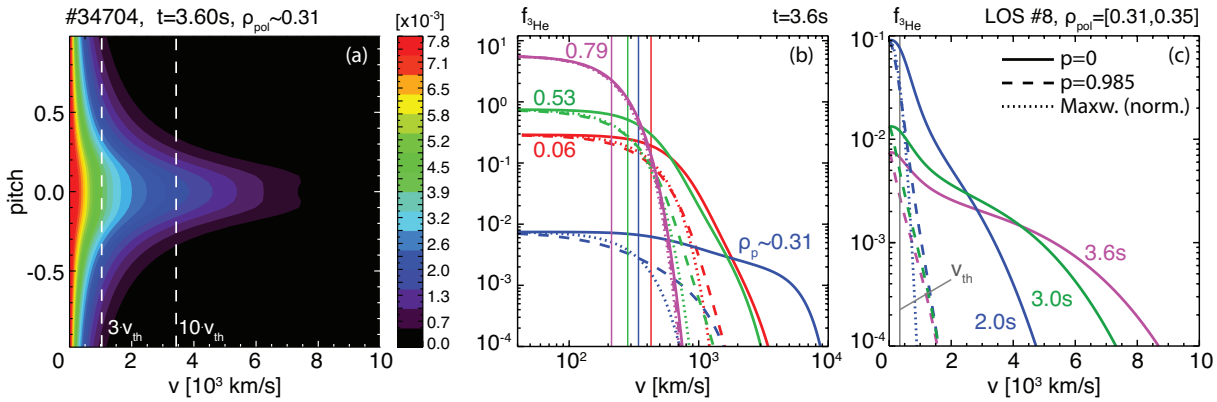

Figure 12: a) Distribution function obtained with TORIC-SSFPQL for #34704 at 3.6 s and $\rho_{pol} \sim 0.3$, assuming $c_{^3\mathrm{He}} = 0.6\%$ and considering FOW effects, b) distribution function for zero pitch angle (——) and for pitch angle of 0.985 (- - - -) for different locations across the plasma radius at 3.6 s and c) for $\rho_{pol} \sim 0.3$ in time. The corresponding Maxwellian distribution functions are also shown (·····).

3.3. Comparison between experimental and forward-modelled CX spectral radiance

The CX spectral radiance that is expected for the distribution function described in the previous section can now be calculated using Eq. (1) and the prediction compared against the experimental measurements for the time points and locations shown in Fig. 5.

The predicted CX radiance is shown as a function of the energy of the ions projected onto the lines-of-sight in Fig. 13, for a distribution function assuming zero-orbit-width (ZOW, dashed lines) and for the distribution function obtained taking into account finite-orbit-width effects (FOW, solid lines). The experimental measurements are shown with circles (faded, for comparison). For t=1.35 s, a Maxwellian distribution function is used. It is readily observed that the CX radiances forward-modelled using TORIC-SSFPQL distribution functions closely approach the measured radiances. The radiance measured at t=1.35 s at $\rho_{\mathrm{pol}} \sim 0.3$ slightly underpredicts the measurement, as the assumed concentration was lower than the measured one at this time point (see Fig. 10). However, the balance between ^{3}He and ^{4}He contributing to the spectrum at the low energies is not well known. Looking at the comparison between the modelled and measured CX spectral radiance at $\rho_{\mathrm{pol}} \sim 0.3$ (corresponding to the RF resonance location) in Fig. 13(a), it is observed that the trend with increasing $\mathrm{P_{ICRF}}$ is opposite. The modelled radiance decreases with increasing ICRF power, while the measurements increase. Accordingly, the agreement is best for the middle $\mathrm{P_{ICRF}}$ case (t=3.0 s). The difference between the modelled $\mathrm{L_{CX}}$ with and without finite-orbit-width effects is small for the different ICRF powers, and smallest for the lowest ICRF power (as the banana orbit width is smaller for lower energy ions).

Comparing the zero-orbit-width prediction (dashed lines) and experiment at different plasma radii in Fig. 13(b), one sees that the predicted signal is ~ 2 times lower than the ones measured by CX at $\rho_{\mathrm{pol}} = 0.31$ and 0.53 in the energy range 10-20 keV. Both the measurement and the prediction show no energetic signal further outside than mid-radius. In contrast to the CX measurement, no energetic helium signal is expected by the

modelling close to the plasma core, as hinted by the $T_{\parallel}$ of this distribution function in Fig. 11. The uncertainty on the experimental radiance is on the order of $\sim 15\%$, in other words the above-mentioned discrepancies are outside the error bars of the measurement. A further uncertainty due to the disturbing emission lines remains as discussed in 2.3. In particular, the flattening of L_{CX} with increasing E_{LOS} at t=3.6 s and $\rho_{pol} \sim 0.31$ is not reflected in the modelling.

The forward-modelling of L_{CX} considers only the ^{3}He distribution function obtained with TORIC-SSFPQL, but does not account for any ^{4}He ions. This is because the balance between the ^{3}He and ^{4}He content in the plasma is unknown. A thermal ^{4}He population will still contribute to the spectral radiance up to energies projected along the line-of-sight of up to 10 keV. For comparison, the spectral radiance at t=1.35 s (no ICRF) can be considered. The implication is that the slope of the spectral radiances for very low energies would not be well reproduced.

Since the ICRF resonance was on the high field side, the trapped particles that have banana orbit tips on the resonance layer, might have orbits with banana widths reaching the region close to the magnetic axis. As discussed, this effect would not be captured in this simulation assuming a zero-orbit-width. Using a distribution function approximately accounting for the finite-orbit-width effects of the energetic ^{3}He ions brings the predicted L_{CX} (solid lines) closer to the measurement. As expected, the main difference observed is the prediction for an energetic ^{3}He ion signal close to the plasma axis and a reduced predicted energetic signal around the plasma mid-radius (Fig. 13(b)), when the more realistic velocity distribution functions accounting for the finite-orbit-width effects are considered.

The forward-modelled spectra obtained using the TORIC-SSFPQL distribution function taking into account finite-orbit-width effects are compared against the measured spectra in Fig. 14. For the case at $\rho_{pol} \sim 0.06$ in Fig. 14(a), the modelled spectrum fits well to the measured one, and the emission lines disturbing the spectrum become more apparent ($\lambda = 470.2 - 470.4$). In Fig. 14(b), the modelled spectrum values on the right wing of the spectrum are lower than the measured ones at $\rho_{pol} \sim 0.31$. The modelling fails to reproduce the measurement at $\rho_{pol} \sim 0.53$ in Fig. 14(c). Failure to reproduce the measurements may involve an error on the magnitude of the ^{3}He population and the balance between energetic and thermal ions, as well as more fine details on the velocity distribution function of the ions.

The predicted spectral radiance across the plasma radius, integrated over two energy ranges (ion energies projected on the lines-of-sight), namely $E_{LOS} = 15 - 20$ keV and 30-35 keV, are compared to the measurement for the three time points with increasing P_{ICRF} in Fig. 15. While the modelling is close to the measurement, key differences are observed. In the case with $P_{ICRF} = 0.9$ MW, the differences between the modelling assuming zero-orbit-widths and that considering finite-orbit-width effects are very small. Adding finite-orbit-width effects still does not explain the measurement close to the plasma core. For the cases with $P_{ICRF} = 1.9$ MW and 2.5 MW, the difference between the zero-orbit-width assumption (dashed lines) and the addition of FOW effects inside $\rho_{pol} \sim 0.2$ is more prominent. But most significantly, the shape of the predicted CX radiance does not match the measured profile. At t=2.0 s ($P_{ICRF} = 0.9$ MW), the measured profile is smoother

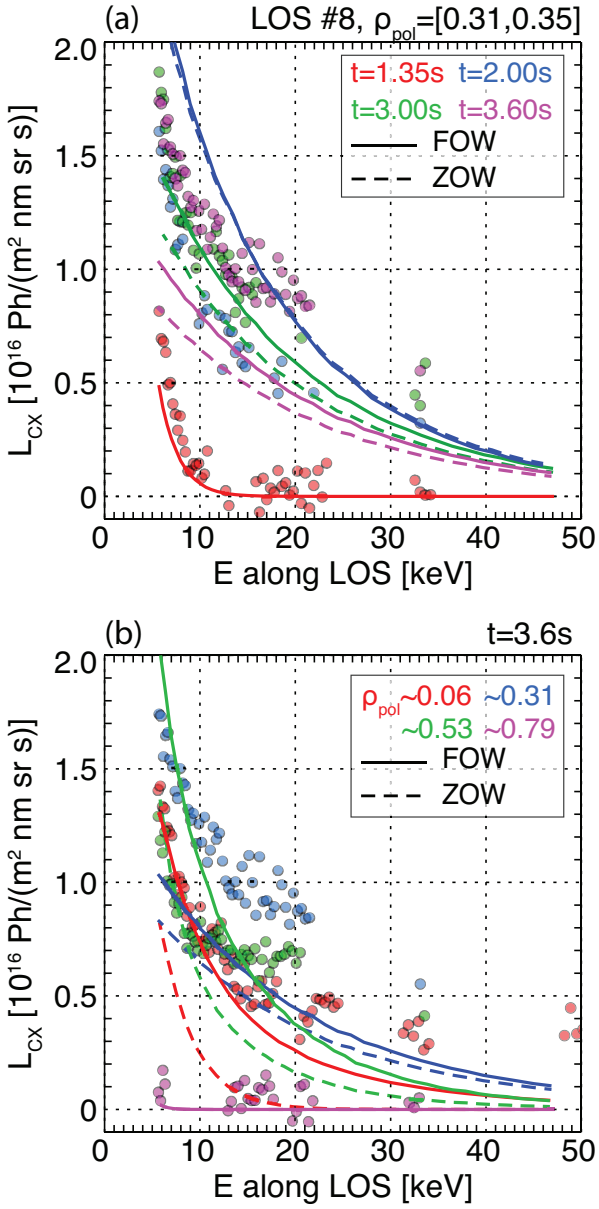

Figure 13: Modelled CX radiance as a function of the ion energy projected on to the line-of-sight using Eq. (1) and TORIC-SSFQPL distribution functions (and a Maxwellian distribution function for t=1.35 s), a) at the time points shown in Fig. 2 at $\rho_{\rm pol} \sim 0.3$ and b) across $\rho_{\rm pol}$ at t = 3.6 s. Both TORIC-SSFPQL distribution functions obtained assuming zero width orbits (ZOW, - - - -) and considering finite width orbits (FOW, ——) are used. The measured CX spectral radiance from Fig. 5 is also shown for comparison.

than the locally peaked predicted profile and reflects a larger population of lower energy ions close to the plasma core than the modelling expects, potentially indicating inward transport of the energetic ions at these energies. At 3.0 s and 3.6 s, $P_{\rm ICRF} = 1.9$ MW and 2.5 MW, respectively, a lower CX signal is predicted around the resonance location

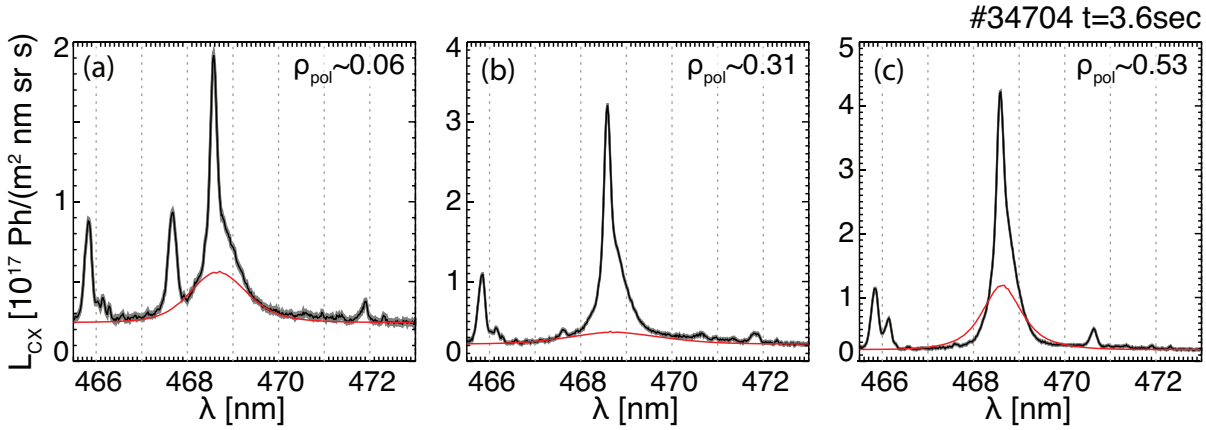

Figure 14: The forward-modelled spectra obtained using the TORIC-SSFPQL distribution function with an estimate for FOW effects (red), compared against the measured spectra (black) in #34704 at t=3.6 s for three lines-of-sight.

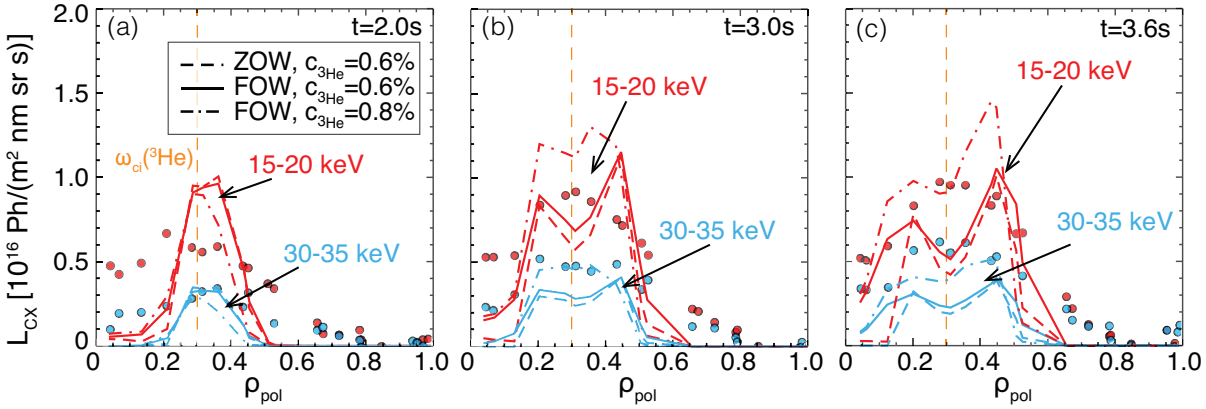

Figure 15: Modelled (lines) and experimental (circles) CX radiances integrated over two energy ranges projected along the line-of-sight ($E_{LOS} = 15 - 20$ keV in red and $E_{LOS} = 30 - 35$ keV in light blue). The predictions using the TORIC-SSFPQL distribution function with ZOW (——) and considering FOW effects (——) are shown. The case assuming a slightly higher ^{3}He concentration of 0.8% and FOW effects is also shown (- - - -). The location of the ^{3}He RF resonance (on the high-field side) is indicated with the vertical dashed line.

($\rho_{pol} \sim 0.3$), as the majority of the ions at this location are accelerated to energies $\gg 50$ keV. However, the reduced energetic signal with respect to the neighbouring radial locations around the resonance location is not observed in the measurement. The measurement reflects a larger population of lower energy ions in this location than the modelling expects. Fig. 16 shows also the cumulative distribution of the energetic helium ions for t = 3.6 s, to confirm that this behavior is observed in the energy range up to 45 keV.

Sawteeth are present in this pulse, with a period of ∼95-105 ms (infrequent enough to be diagnosed by CXRS) and an inversion radius around $\rho_{pol} \sim 0.2$. Fishbones as well as core-localised high-frequency MHD modes are also present. Small differences are noted in the measurement before and after the sawtooth crashes, indicating at least some re-distribution of the fast ions. Comparing time frames with and without fishbones, fewer

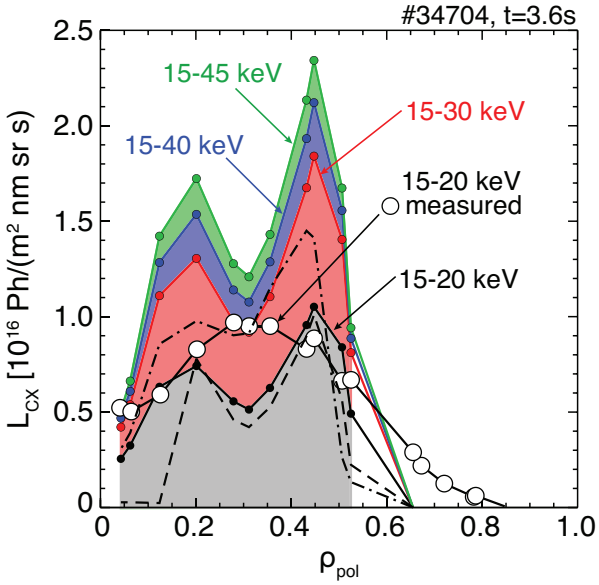

Figure 16: Modelled (full circles and shaded areas) and experimental (open circles) CX radiances integrated over different energy ranges projected along the line-of-sight. The TORIC-SSFPQL distribution function with FOW effects is used (——). The case assuming a slightly higher ^{3}He concentration of 0.8% (- · - · -) and the case assuming a zero banana width and a ^{3}He concentration of 0.6% (- - - -) are also shown for the energy range of 15-20 keV.

energetic helium ions are measured inside the q=1 surface in the presence of fishbones. However, given the 5 ms time resolution of the measurement, the observation is still an average effect. Other mechanisms might also be at play, which act to smooth the strong gradients predicted by the modelling.

The ^{3}He ions with energies $E_{^3He} \gg T_e$ much higher than the electron temperature will not be affected by turbulence. One can attempt to roughly estimate the effect of turbulence on these energetic ^{3}He ions by utilising Eq. (35) in [20], valid for fusion-born α-particles with energies E_α in the range $23 < E_\alpha/T_e < 700$. An energetic ^{3}He ion with $T_\parallel \sim 200$ keV and $T_\perp \sim 15$ keV, as those predicted at $\rho_{pol} \sim 0.45$ at t = 3.6 s (see Fig. 11), has an equivalent temperature of ~ 138 keV, i.e. $E_{^3He}/T_e \sim 92$. Applying the equation, it is obtained that the turbulent diffusion of such ions is approximately 10% times that of thermal helium ions. While much smaller, turbulence cannot be ruled out from playing a role in the re-distribution of the energetic ^{3}He ions measured here. Further detailed transport modelling is required to assess the turbulent transport of the fast ^{3}He ions, in particular considering the velocity distributions of these RF-accelerated ions.

As discussed earlier, the ^{3}He concentration is not exactly known, but is an important input to the modelling. Therefore, the influence of the assumed ^{3}He concentration on the predicted spectra was assessed. The effect of using a slightly higher concentration of $c_{^3He} = 0.8\%$ is shown with dashed-dotted lines in Fig. 17, in comparison to the modelled radiance using $c_{^3He} = 0.6\%$ (with solid lines). The higher concentration assumption leads to a slightly better agreement at 1.35 sec at $\rho_{pol} \sim 0.3$ when ICRF is not applied. Better

agreement is also found close to the plasma axis and at the resonance location ($\rho_{\mathrm{pol}} \sim 0.3$), but the predicted signal at mid-radius is now lower than the measured value, as seen in Fig. 17(b). Similarly, the slightly higher concentration does not provide a perfect agreement for all time points in the pulse in Fig. 17(a). A better agreement is obtained for the highest $\mathrm{P_{ICRF}}$. Looking back to Fig. 15, the increased helium concentration has only a very small effect at t=2.0 s, while it changes the expected radiance for $\mathrm{E_{LOS}} = 15 - 20$ keV and $30 - 35$ keV at t=3.0 s and 3.6 s (dash-dotted line). The reduced radiance levels expected at the resonance location is not as pronounced, but an increase radiance is still expected further outside in the highest $\mathrm{P_{ICRF}}$ case.

These observations support the argument that the ^{3}He concentration is a critical parameter for the assessment of the modelling capabilities to reproduce the experimental measurement. Not only the value of the ^{3}He concentration, but also the assumption of a flat helium concentration profile used as input to the TORIC-SSFPQL modelling plays a role. Regardless all these uncertainties, the ICRF scenario is rather robust for plasma heating. However, the input ^{3}He concentration alone cannot explain the shape of the CX radiance profiles. The following elements are also important to the comparison between experimental and modelled CX signals due to the energetic ^{3}He population: the uncertainty on the experimental measurement (discussed in Sec. 2), the uncertainties in the modelled spectral radiance beyond the velocity distribution function, and the approach used to take into consideration the banana orbits of the energetic ions.

Each variable in Eq. (1) is connected with its own uncertainty. The uncertainties on the kinetic profiles enter the calculation of the distribution function, the collision velocity between the ions and the beam neutrals, the atomic data, and the beam neutrals density. The uncertainty in the density of the beam neutrals $n_b^{E,m}$ includes furthermore the uncertainty in the neutral beam power reaching the plasma, for example due to losses at the NBI duct, as well as uncertainties in the exact geometry and width of the neutral beam [16]. The quantification of uncertainties of the atomic data, namely the CX emission rates but also the atomic data entering the calculation of the beam neutral density, is not straightforward and usually ignored. The CXRS measurement locations and line-of-sight paths are well characterised and the effective measurement location of each line-of-sight when more than one neutral beams are injected is used, with an average uncertainty in the radial location of $\pm$1.7cm. However, the magnetic equilibrium reconstruction, needed to calculate the angles to the magnetic field lines, is increasingly less accurate towards the plasma core. These uncertainties contribute to the uncertainty on the modelled CX radiance, but cannot explain the discrepancies between experiment and modelling.

The TORIC-SSFPQL modelling can be further constrained by utilising the fast ion loss model available in the code. However, identifying the correct parameters for this is not straightforward. Furthermore, the limits of a numerical algorithm such as SSFPQL need to be acknowledged, and a Monte Carlo approach can be considered. Finally, the modelling presented here cannot account for physics mechanisms such as turbulence or MHD activity that might be responsible for the radial redistribution of the energetic ions.

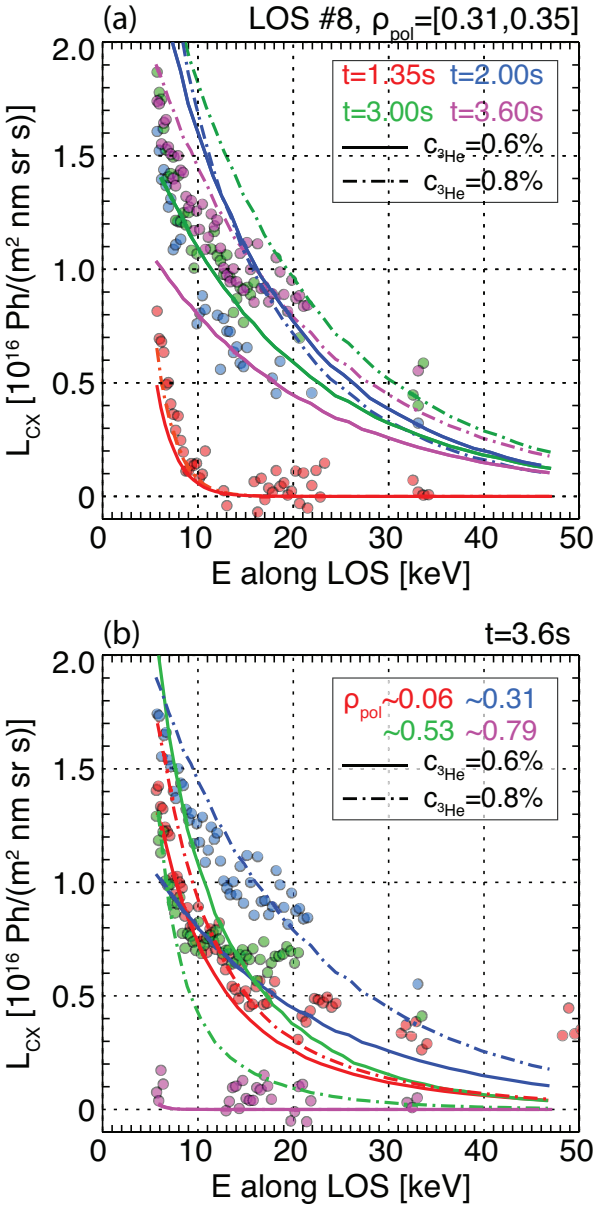

Figure 17: Modelled CX radiance as a function of the ion energy projected on to the line-of-sight using Eq. (1) and TORIC-SSFQPL distribution functions (and a Maxwellian distribution function for t=1.35 s), a) at the time points shown in Fig. 2 at $\rho_{\mathrm{pol}} \sim 0.3$ and b) across ρ_{pol} at $\mathrm{t} = 3.6$ s. TORIC-SSFPQL distribution functions obtained with an estimate for the FOW effects, for $c_{^3\mathrm{He}} = 0.6\%$ (——) and $c_{^3\mathrm{He}} = 0.8\%$ (- - - -) are used. The measured CX spectral radiances from Fig. 5 are also shown for comparison.

4. Discussion and outlook

CXRS measurements of energetic ^{3}He ions at AUG, heated with the three-ion ICRF scenario which preferentially accelerated ^{3}He ions in H-D mixed plasmas, are presented.

^{3}He ions with energies parallel to the lines-of-sight of up to ~ 35 keV can be detected. The measured CX spectra are compared with forward-modelled spectra evaluated using TORIC-SSFPQL distribution functions. The magnitude of the predicted CX spectral radiance and the expected energies of the ions that undergo CX agree well enough with the measurement to confirm that the wings in the CX spectra are due to ICRF-accelerated fast ^{3}He ions. However, several discrepancies between the experimental measurement and the forward-modelling illuminate details of the velocity distribution function of the energetic helium ions.

TORIC-SSFPQL modelling that takes into account the ion banana orbits by performing an average over the orbits ameliorates the comparison between the experiment and the modelling. The output of the modelling and the comparison to the measurement strongly depends on this estimate and on the ^{3}He concentration used as input to the modelling. Further iterations of the modelling with different assumptions on both the magnitude and peaking of the ^{3}He concentration can be employed to pinpoint the velocity distribution of the helium ions. Discrepancies between the measurement and the modelling prediction presented here indicate that other physics mechanisms that influence the phase-space distribution of the ions are necessary to explain the measurements, for example orbit losses, radial fast ion transport (possibly RF-induced), or MHD activity, and a more complete treatment of the finite orbit widths might need to be considered.

Measurements of this type can be extended by sampling different parts of the energetic ^{3}He velocity distribution function, utilising lines-of-sight with different viewing directions (angles to the magnetic field lines). Employing such measurements, a tomographic reconstruction of the velocity distribution becomes possible, as done in [21] for deuterium NBI fast ions. Depending on the flexibility of the three-ion ICRF scenario, as a tool to create the energetic helium population, energetic helium transport studies in current devices can be envisaged. These type of studies can include the behavior and slowing down of the energetic helium ions in different plasma conditions and collisionality regimes, and the redistribution of energetic helium ions due to sawteeth.

Such measurements of energetic helium ions provide a way to study confined fast ions without restricting the studies to deuterium. The mass and charge of the fast ions enter a number of fast ion parameters, such as the slowing-down time and the gyro-radius, and subsequently define the confinement and prompt losses of the fast ions. The neoclassical and turbulent transport of the fast ions depend on their charge and mass. Furthermore, the effect of the fast ions on the plasma turbulence depends on the fast ion species and the characteristics of their velocity distribution function. Investigating ^{3}He ions implies that only the difference in mass remains with respect to the fusion-produced ^{4}He.

The space-velocity distribution function of the ICRF accelerated ^{3}He ions does not directly compare to that of fusion-produced helium in the plasma core. However, with the three-ion ICRF scenario, the ^{3}He ions reach energies clearly larger than those typically achieved with other heating schemes (ICRF, NBI, and possible synergies [6]), which also involve different ion species. As a means to produce fast ions, the three-ion ICRF scenarios allow more realism in the experimental investigations of the impact of fusion-born α-particles on transport (e.g. turbulence, Alfvénic activity, and their interplay), for extrapolations to fusion reactors [22].

As shown here, CXRS can provide important information on the confined energetic helium ions, which in combination with lost fast ion diagnostics can be used for validation of fast ion and ICRF modelling codes for use in current and future devices. Comparing the results of the advanced ICRF modelling possible with the extensions to the TORIC-SSFPQL code against the experimental measurements can significantly contribute to the advancement of the modelling capabilities. The modelling assists in the interpretation of the measurement, and the measurement itself can provide a test-bed for modelling assumptions and thus elucidate the behavior of the energetic helium ions in the plasma.

Acknowledgment

This work has been carried out within the framework of the EUROfusion Consortium and has received funding from the Euratom research and training programme 2014-2018 and 2019-2020 under grant agreement No 633053. The views and opinions expressed herein do not necessarily reflect those of the European Commission.

References

[1] G.R. McKee *et al*, Nucl. Fusion **37**, 501 (1997)
https://doi.org/10.1088/0029-5515/37/4/i08
[2] M.G. von Hellermann *et al*, Plasma Phys. Control. Fusion **35**, 799 (1993)
https://doi.org/10.1088/0741-3335/35/7/002
[3] M.J. Mantsinen *et al*, Phys. Rev. Lett. **88**, 105002 (2002)
https://doi.org/10.1103/physrevlett.88.105002
[4] B.C. Stratton *et al*, Nucl. Fusion **34**, 734 (1994)
https://doi.org/10.1088/0029-5515/34/5/i02
[5] Ye.O. Kazakov *et al*, Nat. Phys. **13**, 973 (2017)
https://doi.org/10.1038/nphys4167
[6] R. Bilato *et al*, Nucl. Fusion **51**, 103034 (2011)
https://doi.org/10.1088/0029-5515/51/10/103034
[7] R.J. Fonck *et al*, Phys. Rev. A **29**, 3288 (1984)
https://doi.org/10.1103/physreva.29.3288
[8] A. Kappatou *et al*, Plasma Phys. and Control. Fusion **60**, 055006 (2018)
https://doi.org/10.1088/1361-6587/aab25a
[9] U. Gerstel *et al*, Plasma Phys. Control. Fusion **39**, 737 (1997)
https://doi.org/10.1088/0741-3335/39/5/005
[10] Ye.O. Kazakov *et al*, 27th IAEA Fusion Energy Conference, EX/8-1 (2018)
https://www.iaea.org/sites/default/files/18/10/cn-258-abstracts.pdf
[11] Ye.O. Kazakov *et al*, submitted to Phys. Plasmas (2020)
[12] M. Schneider *et al*, EPJ Web Conf. **157**, 03046 (2017)
https://doi.org/10.1051/epjconf/201715703046
[13] S.K. Rathgeber *et al*, Plasma Phys. Control. Fusion **52**, 095008 (2010)
https://doi.org/10.1088/0741-3335/52/9/095008
[14] W.W. Heidbrink *et al*, Plasma Phys. Control. Fusion **49**, 1457 (2007)
https://doi.org/10.1088/0741-3335/49/9/008
[15] B. Geiger *et al*, Rev. Sci. Instrum. **84**, 113502 (2013)
https://doi.org/10.1063/1.4829481
[16] R. McDermott *et al*, Plasma Phys. Control Fusion **60**, 095007 (2018)
https://doi.org/10.1088/1361-6587/aad256

[17] M. Salewski *et al*, Plasma Phys. Control. Fusion **56**, 105005 (2014)
https://doi.org/10.1088/0741-3335/56/10/105005
[18] M. Brambilla, Plasma Phys. and Control. Fusion **41**, 1 (1999)
https://doi.org/10.1088/0741-3335/41/1/002
[19] M. Brambilla, Nucl. Fusion **34**, 1121 (1994)
https://doi.org/10.1088/0029-5515/34/8/i06
[20] C. Angioni, A.G. Peeters, Phys. Plasmas **15**, 052307 (2008)
https://doi.org/10.1063/1.2913610
[21] M. Weiland *et al*, Nucl. Fusion **57**, 116058 (2017)
https://doi.org/10.1088/1741-4326/aa7e0a
[22] S. Mazzi *et al*, to be submitted to Nat. Phys. (2020)